ACS Photonics

Article

pubs.acs.org/journal/apchd5

Plasmonic Enhancement of Infrared Vibrational Signals: Nanoslits versus Nanorods

Christian Huck,[†] Jochen Vogt,[†] Michael Sendner,[†,‡] Daniel Hengstler,[†] Frank Neubrech,[†,§] and Annemarie Pucci*[,†,‡]

[†]Kirchhoff Institute for Physics, University of Heidelberg, Im Neuenheimer Feld 227, 69120 Heidelberg, Germany

[‡]InnovationLab GmbH, Speyerer Straße 4, 69115 Heidelberg, Germany

[§]4th Physics Institute and Research Center SCoPE, University of Stuttgart, Pfaffenwaldring 57, 70569 Stuttgart, Germany

Supporting Information

ABSTRACT: We report on systematic investigations of plasmonically active nanoslits as a beneficial substrate for surface-enhanced infrared absorption (SEIRA). Arranged in arrays, nanoslits with the proper geometry feature strong nanorod-like resonances in the infrared spectral range, as predicted by Babinet's principle for the same geometrical dimensions. SEIRA enhancement as studied with a thin self-assembled molecular layer of octadecanethiol reaches the values obtained with nanorods if the slit geometry is optimized. We show by systematically examining the important parameters that the slit width has an especially strong influence on the near-field intensity and therefore on the SEIRA signal. Furthermore, the transversal and longitudinal couplings of nanoslits are studied. Compared to nanorod arrays, a stronger influence of the array periodicities on the plasmonic excitations is observed, which indicates coupling via surface plasmon polaritons. So the array periodicity could be further optimized toward higher SEIRA signals. Our results give access to general design rules for sensing applications based on the use of inverse nanostructures.

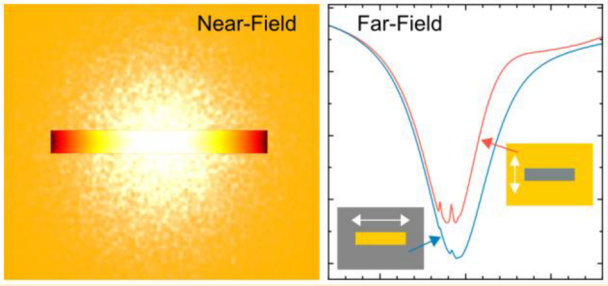

KEYWORDS: *infrared, plasmonics, Babinet's principle, inverse nanostructures, surface-enhanced infrared absorption, SEIRA*

During the last 20 years metal nanoparticles have attracted a lot of interest due to their ability to confine light in a nanometric volume. This property leads to interesting applications such as the use of plasmonic nanoparticles as optical sensors.[1−4] This concept is based on the idea of bringing molecular species to the hot spots of the nanoparticles, where the electromagnetic near-field intensity is enhanced by several orders of magnitude.[5] By following this approach, the low interaction cross sections of Raman or IR excitations can be dramatically increased and the detection of minute amounts of molecules enabled, down to single-molecule detection in the case of surface-enhanced Raman spectroscopy (SERS).[6−8] In order to further lower the detection limit, nanoparticles with different kinds of geometries and arrangements were investigated. The most prominent examples are linear nanorods acting (and named) as nanoantennas, which can enhance the signals of molecular vibrations by up to 5 orders of magnitude.[9] The SEIRA enhancement of such linear antennas is further improved by using nanoantenna dimers, separated by nanometer-sized gaps, as it was shown several times.[10−12] Other approaches are the use of log-periodic trapezoidal optical antennas that serve as a multifrequency optical antenna designed to operate with a bandwidth of several octaves[13] and the use of split ring resonators.[14] Other promising platforms for SEIRA measurements are nanostructures above reflective substrates.[15] For example, it was recently shown that fan-shaped gold nanoantennas above a reflective gold mirror with a silicon dioxide spacing layer lead to a vibrational signal enhancement of up to 5 orders of magnitude.[16] A different approach for the use of nanoparticles above a reflective substrate is the elevation of the nanostructures by etching of the underlying substrate via wet-chemical[17] or dry etching processes.[18−20] It was reported that the accessible near-field area is increased and the SEIRA enhancement can be improved by more than 1 order of magnitude by following this approach.[21]

All these concepts have one in common, namely, the use of solid metal nanoparticles. However, it is well known that so-called inverse nanostructures, consisting of nanoapertures in a continuous metallic film, also feature plasmonic resonances, according to Babinet's principle.[22−28] The first use of inverse H-shaped nanoapertures as a substrate for SEIRA was recently shown;[29] nevertheless, several fundamental questions regarding inverse nanostructures still remain.

In this contribution we systematically investigate the use of inverse nanoantennas (nanoslits) as a substrate for SEIRA. We directly compare the far-field response of nanoslit arrays with

Received: July 15, 2015
Published: September 8, 2015

DOI: 10.1021/acsphotonics.5b00390
ACS Photonics 2015, 2, 1489−1497

that of nanoantenna arrays via infrared microspectroscopy. In order to investigate the SEIRA activities of the two plasmonic systems, a self-assembled molecular monolayer of octadecanethiol (ODT) was prepared on the nanostructures, and the enhanced vibrational signals of the ODT molecules were evaluated. For a better understanding, an additional insight into the near-field distributions is given by finite-difference time-domain (FDTD) simulations. Finally, we discuss the influence of the geometry parameters, most importantly the width w, of the nanoslits, and of the coupling behavior of nanoslits arranged in arrays on the SEIRA signal enhancement. From our results we derive general design rules for the optimum nanoslit geometry and arrangement for sensing applications.

RESULTS AND DISCUSSION

The nanoslit fabrication consists of a standard electron beam lithography (EBL) process and subsequent argon-ion milling, which is depicted in Figure 1a. By using the patterned poly(methyl methacrylate) (PMMA) layer as an etching mask for the argon-ion milling process, nanoslit structures with various dimensions are fabricated (see Methods for details). The use of an EBL process combined with subsequent argon-ion milling has major advantages compared to the preparation of inverse nanostructures by using a focused ion beam (FIB).[28,30] The preparation of large arrays is possible on reasonable time scales, and the preparation of tiny structures with dimensions of less than 20 nm is achieved with standard approaches also for thick Au layers. A scanning electron microscope (SEM) image of such a nanoslit array (w = 50 nm, L = 3000 nm, Δ_x = 4000 nm and Δ_y = 5000 nm, as indicated in the figure) etched in a 50 nm Au layer is shown in Figure 1b. The polycrystalline Au surface is nicely visible. To determine the etching depth of the structures, additionally, atomic force microscopy (AFM) measurements have been carried out. The measurements reveal that the nanoslits have a depth of approximately 75 nm, indicating that not only the Au layer but an additional 25 nm of the underlying calcium difluoride (CaF_2) substrate have been removed. Figure 1c depicts the full geometry information including a molecular layer, used for the SEIRA studies of ODT.

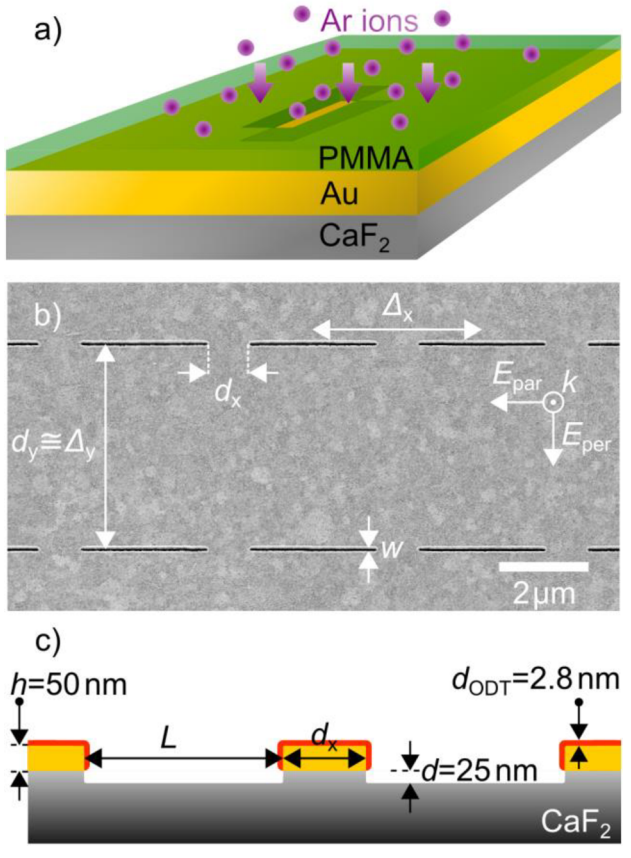

Figure 1. (a) Schematic illustration of the fabrication process: Nanoslits are produced by Ar-ion milling of a 50 nm Au layer through a PMMA mask. (b) SEM image of a gold nanoslit array on a CaF_2 substrate. The separation distances d_x and d_y, the periodicities Δ_x and Δ_y, and the width w are indicated. The orientation of the electric field vector (E) is usually set perpendicular (E_{per}) to the long slit axis to excite the nanoslit plasmon resonance. (c) Cross section of a nanoslit array (cut through a nanoslit) covered with a monolayer of ODT depicting the geometry used for FDTD calculations.

The infrared (IR) optical properties of different nanoslit and nanoantenna arrays were investigated by micro-IR spectroscopy (see Methods for details) in reflectance (nanoslits) or transmittance (nanoantennas) geometry. According to Babinet's principle, several quantities exchange their respective roles in the inverse nanoslit system, which has to be taken into account when exciting the nanoslit array: Instead of a broad peak in transmittance, the nanoslits will feature a similar peak shape in reflectance geometry. Furthermore, instead of polarizing the light parallel to the long axis, as is the case for a solid antenna, a slit features a similar resonance when using light polarized perpendicular to the long slit axis. The two polarization directions are indicated in Figure 1b. The electric and magnetic field components change their roles, resulting in a near-field distribution exhibiting a dipolar pattern in the magnetic component for the nanoslit instead of a dipolar pattern in the electric component, as is the case for the nanorod. It is important to mention that Babinet's principle neglects light absorption and assumes that all objects are perfect electrical conductors with a vanishing skin depth δ_{Skin},[31] which is only a rough approximation in the case of gold with $\delta_{Skin} \approx$ 25 nm in the infrared. In order to approach Babinet's assumptions, the gold should be sufficiently thick and any defect-related damping should be avoided. It should also be noticed that Babinet's principle does not hold for any kind of near-field interaction, which often has to be considered for plasmonic nanoparticles. Figure 2a shows the IR optical response of nanoslit arrays with different lengths L ranging from 0.75 to 3.0 μm covering the whole mid-IR spectral range. For light polarized along the short axis, sharp resonances are excited, as predicted by Babinet's principle. In addition, the figure shows the response to parallel polarized light, where a 100% line without any excitation is observed. In the inset of the figure the relationship between the slit length and the resonant wavelength is shown. The relationship is perfectly linear, as already described in ref 28, and it is well known from solid nanoantennas in the infrared.[32,33]

When comparing the transmittance spectrum of a nanoantenna array with the reflectance spectrum of a nanoslit array of exactly the same dimensions (Figure 2b), one notes a remarkable similarity: First of all, both structures feature a similar resonance frequency, as predicted by Babinet's principle. The similarity also holds for the extinction and the quality factor, which is defined as the resonance frequency ω_{res} divided by the full width at half-maximum Γ, $Q = \omega_{res}/\Gamma$. This fact cannot be exactly expected when referring to Babinet's

DOI: 10.1021/acsphotonics.5b00390
ACS Photonics 2015, 2, 1489−1497

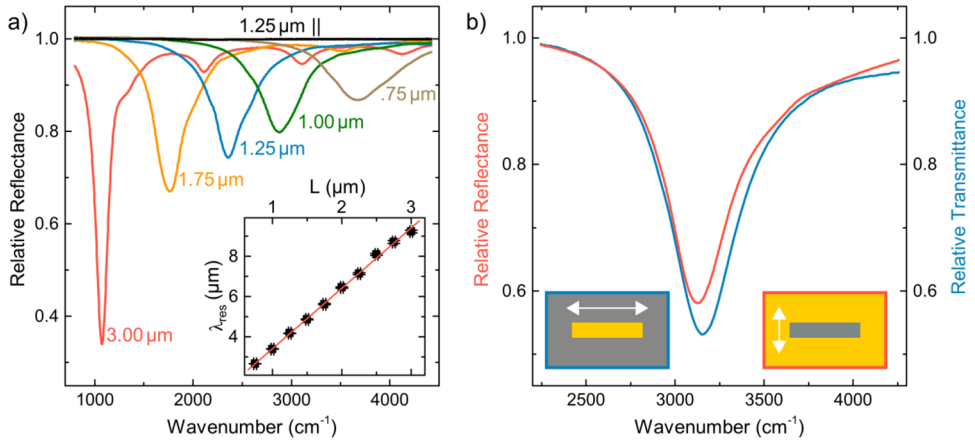

Figure 2. (a) Selection of experimental relative reflectance spectra of nanoslit arrays with dimensions w = 50 nm, d_x = 1 μm, d_y = 5 μm, and varying length L, as indicated. For the nanoslit array with a length of 1.25 μm the excitation with light polarized parallel (||) to the long slit axis is also shown. In this case a 100% line is observed. The inset shows the perfect linear relationship between the resonant wavelength λ_{res} and the length L. (b) Comparison of a nanoslit array with a nanoantenna array with the same dimensions (w = 50 nm, L = 900 nm, Δ_x = 2.6 μm, Δ_y = 1.7 μm). The different excitation polarizations are indicated in the sketches by white arrows.

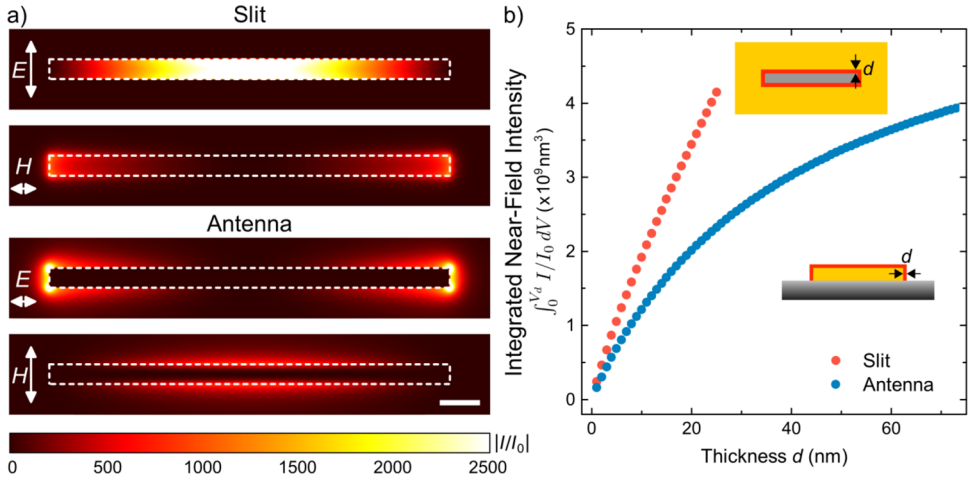

Figure 3. (a) Near-field intensity distribution of a resonantly excited nanoantenna array as well as a nanoslit array in a plane parallel to the substrate at half height of the nanoslit/nanoantenna: The solid nanoantenna features an enhanced near-field distribution in the vicinity of the nanoantenna when excited with light polarized with the electric field vector parallel to the long antenna axis. In contrast, according to Babinet's principle, the inverse nanoslit features an enhanced electromagnetic near-field when excited with light polarized with the magnetic component parallel to the long slit axis. The E-field of the nanoantenna features two hot spots at the tip ends with an extent of some 10 nm, whereas the nanoslit features only one hot spot, strongly confined in the slit, with a much bigger extent (scale bar: 100 nm). (b) Near-field intensity integrated over a shell volume surrounding the nanostructure (see inset) with increasing thickness d. The integrated intensity of the nanoslit has a higher value for all thicknesses d, until the nanoslit is completely filled ($d = w/2$).

principle, because the predictions of the principle apply only for the light scattering by the structures. However, plasmonic extinction in the infrared always consists of two contributions, plasmonic scattering and plasmonic absorption.[34] Depending on the exact geometry (mainly the width and height), the plasmonic absorption of light can even dominate over the amount of scattered light. Nevertheless, the similarity of both kinds of plasmonic spectra shown in Figure 2b is remarkably good.

When considering nanoslits as a substrate for sensing applications, such as SEIRA, it is important to characterize the near-field distribution of a nanoslit. Although the far-field responses of a nanoantenna and a nanoslit are very similar, as shown in Figure 2b, the spatial distributions of the near-field enhancement are totally different. A comparison of the enhanced near-field of a nanoantenna and a nanoslit array with typical dimensions (L = 1000 nm, w = 50 nm, Δ_x = Δ_y = 1.7 μm) for both the electric and the magnetic near-field intensity is shown in Figure 3a. All near-fields were normalized to the incoming electric or magnetic field intensities, respectively. When looking at the electric field component, it is visible that the antenna features two distinct hot spots at the tip ends of the nanoantenna. In contrast, the nanoslit features only one hot spot located in its center. However, the single hot spot of the slit is much more extended, compared to the solid nanoantenna, and has a nearly constant value of the electric field intensity over the width of the slit (see also Figure S1 in the Supporting Information). Moreover, the E-field of the slit is exclusively located inside the slit, yielding a near-field compression when decreasing the width of the slit. This will be discussed later on. The nanoslit array as well as the nanoantenna array feature a maximum field intensity enhance-

DOI: 10.1021/acsphotonics.5b00390
ACS Photonics 2015, 2, 1489−1497

ment I/I_0 of approximately 2500. The distribution of the magnetic field components behaves the other way around: The magnetic component of the nanoslit is reminiscent of the electric component of the antenna, with two magnetic hot spots at the tip ends of the slit. The magnetic component is highest inside the slit; however a non-negligible part extends into the gold layer. The similarity of the magnetic dipole aligned parallel to the long nanoslit axis to the electric dipole along the long nanoantenna axis can be interpreted as a magnetic character of the nanoslit.[28] Vice versa, the magnetic component of the nanoantenna is reminiscent of the electric component of the slit.

Due to the different electrical field distributions of the two structures, it is hard to judge from Figure 3a directly whether a nanoslit or a nanoantenna promises the better field distribution for sensing applications. When considering molecular layers surrounding the structure, e.g., self-assembled monolayers, evaporated films, or spin-coated layers, this question can be answered by integrating the electrical near-field intensity in a volume surrounding the slit/antenna up to a certain distance d. This is shown in Figure 3b. The inset indicates the volumes over which the field intensities were integrated: For the antenna the integration volume was increased in every direction except the direction in which the substrate is located. For the nanoslit only the volume inside the nanoslit was considered. The evolution of the curve for the antenna shows a strong increase for small distances and decreasing slope with increasing distance. A similar trend of the near-field has already been experimentally extracted in ref 35 from in situ SEIRA measurements of thin molecular layers during the growth of the probe layer. The development of the integrated near-field with d for the nanoslit is different. For small distances d the integrated near-field intensity increases as steep as that for the solid nanoantenna. However, whereas the slope of the nanoantenna starts decreasing with increasing thickness, the slope of the integrated near-field intensity of the nanoslit stays at a nearly constant value. This behavior expresses once more that the near-field intensity is nearly constant over the width of the nanoslit. The constant increase of the near-field intensity is of particular interest for the enhancement of large molecules, such as proteins, where the important sensing area can reach extensions of 10 nm or even more. The slit gives higher integrated near-field intensities for all distances d, until it is completely filled with the probe layer. Additionally, we have to mention that the integrated volume of the nanoantenna is much larger than that of the slit because the nanoantenna has an additional surface (top surface) that was considered for the integration. When normalizing the curve to the volume, which means looking at the average near-field intensity, the advantages of the slit dominate even more.

In order to demonstrate the superiority of the nanoslit over the nanoantenna, a monolayer of ODT has been prepared on a sample containing nanoslit arrays (with various lengths, Δ_x, and Δ_y) and, for comparison, also on a sample containing nanoantenna arrays (see Methods for details of the adsorption procedure). ODT forms a homogeneous layer on the gold surfaces of the samples with a thickness of approximately 2.8 nm (see also Figure 1c). In contrast to an evaporated or spin-coated molecular layer, ODT has the advantage that the distribution of the molecule inside of nanoslits can be predicted, as it will cover all side walls of the nanoslits. It is also well suited for our investigations because it features several IR-active vibrational modes between 2800 and 3000 cm^{-1}, originating from the symmetric and asymmetric stretching vibrations of the methyl (CH_3) and the methylene (CH_2) groups. After the monolayer was prepared, the samples were immediately characterized by means of IR microspectroscopy.

Figure 4 shows the IR response of a representative antenna and slit array. As discussed before, the slit (antenna) array

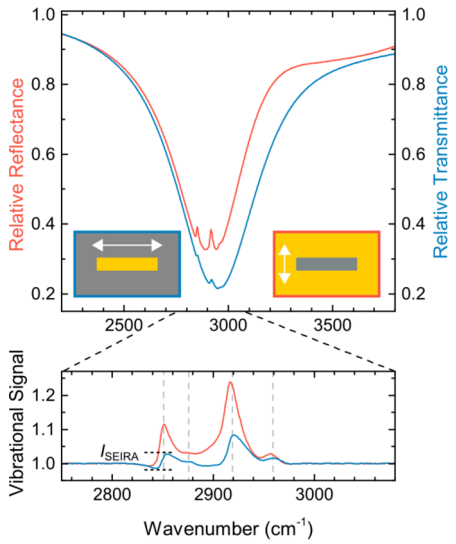

Figure 4. Relative IR reflectance (transmittance) of a nanoslit (nanoantenna) array covered with a monolayer of ODT. The dimensions of both arrays are w = 50 nm, $\Delta_x = \Delta_y$ = 1.7 μm, and L_{Slit} = 1000 nm ($L_{Antenna}$ = 1050 nm). The lower panel shows the baseline-corrected vibrational signal of the ODT molecule. The peaks can be attributed to the symmetric and asymmetric stretching vibrations of the CH_2 and CH_3 groups of ODT (indicated by dashed vertical lines).

features a strong plasmonic resonance when excited with light polarized perpendicular (parallel) to the long axis of the nanostructure. The plasmonically enhanced vibrations of ODT can be seen as dips in the spectrum. In both cases the dips are pointing upward, which can be explained by coupling of the plasmonic excitation with the vibrational one, leading to a Fano-type line shape.[9,36] For the quantitative analysis the vibrational signals of ODT have been separated from the plasmonic excitation by dividing the spectrum by the plasmonic baseline, which was estimated using an asymmetric least-squares smoothing algorithm proposed by Eilers (see refs 4, 12, 37 for details). The baseline-corrected vibrational signal is shown in the lower panel of Figure 4. The vibrational signal size of the asymmetric CH_2 stretching vibration (2920 cm^{-1}) of the nanoslit array has a size of approximately 23.9%, whereas the nanoantenna array produces a signal of only 8.4%. The difference of the two signals is even bigger than expected from the integrated near-field intensities shown in Figure 3. Concerning the simulation one reason might be the fact that the near-field integration of the nanoslit does not consider the area on top of the Au layer. In the experiment ODT molecules will also adsorb on these sites. However, the near-field intensity is very low at these sites and, additionally, the same amount of ODT is adsorbed on the Au mirror used for the reference measurement. Therefore, the contribution of these molecules to the vibrational signal can safely be neglected. Furthermore, the SEIRA line shape for the two experiments is slightly

DOI: 10.1021/acsphotonics.5b00390
ACS Photonics 2015, 2, 1489−1497

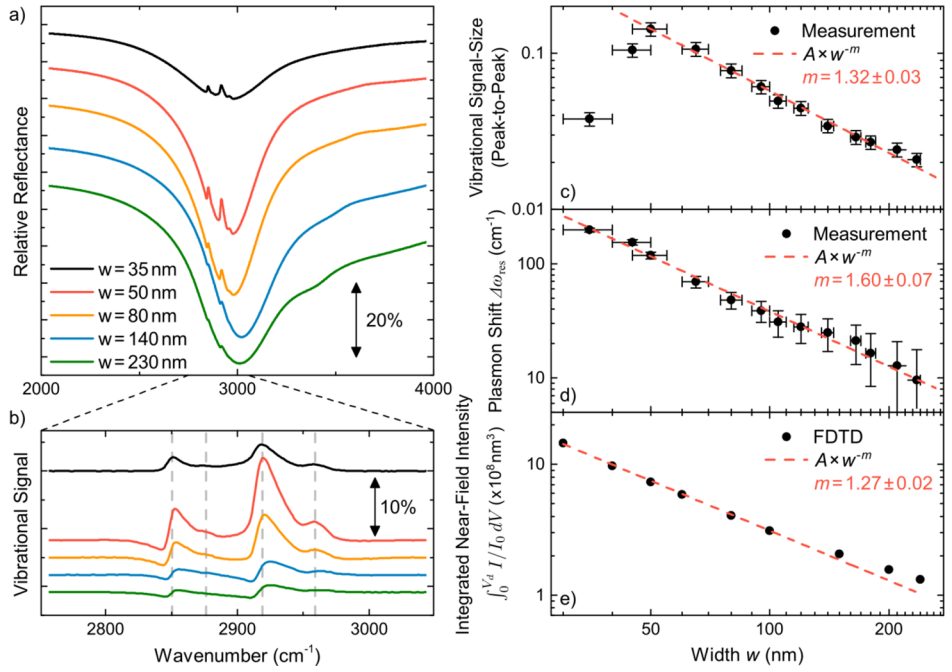

Figure 5. Influence of the slit width w on the SEIRA enhancement: Relative reflectance (a), baseline-corrected vibrational ODT signal (b), vibrational signal strength of the asymmetric CH_2 stretching vibration (2920 cm^{-1}) (c), and the shift of the plasmon resonance frequency due to the ODT layer (d) of nanoslit arrays with varying width w. The vibrational signal of ODT and the shift of the plasmonic resonance frequency strongly increase with decreasing width w, due to a stronger electrical field confinement. (e) Near-field intensity integrated over the area where ODT is adsorbed (3 nm layer, see also Figure 3 for comparison) with respect to the slit width w.

different, indicating marginal differences in the plasmonic coupling.

The enhancement factor (EF) for the nanoslits is estimated according to the relation

$$\mathrm{EF} = \frac{I_{\mathrm{SEIRA}}}{I_{\mathrm{ref}}} \times \frac{A_{\mathrm{unit}}}{A_{\mathrm{ODT}}} \qquad (1)$$

where $A_{\mathrm{unit}} = \Delta_x \times \Delta_y$ is the area per slit, $A_{\mathrm{ODT}} \approx 2 \times L \times h$ is the whole area inside the slit covered with ODT (almost the elongated side walls of the slit, see also Figure 3a), I_{SEIRA} is the peak-to-peak value (difference between the minimum and the maximum of the asymmetric Fano-type signal, see Figure 4 and ref 4) of the baseline-corrected vibrational signal, and I_{ref} is the signal observed in the reference measurement that was carried out in IR reflection-absorption (IRRAS) geometry. The reference signal I_{ref} was corrected since the IRRAS geometry already provides an enhancement due to the mirror-dipole effect and the grazing incidence of light.[9] This results in an average EF of 13 500. Another approximate relation with $A_{\mathrm{ODT}} = 2 \times w \times h$ is used to calculate the EF for the nanoantenna, leading to a value of 93 400 for our solid polycrystalline antennas. Even though the vibrational signal size with the nanoslits is a factor of 3 higher, the estimated enhancement factor is lower because of the 20 times bigger hot spot area A_{ODT} used in the denominator of eq 1. For the calculation of the maximum EF, the near-field distribution in the slit (see Figure S1) should be considered. Nevertheless, for sensing applications, the advantage of the slit is clearly the larger hotspot, which can gather more molecules than an apex of a nanorod, which finally gives a higher SEIRA signal for the same adsorbate density; see Figure 4.

In the following we will optimize the SEIRA response of the nanoslit arrays by tailoring the geometric parameters. First, the width w of the slits is varied as the most important quantity for the near-field strength, whereby the separation distances are fixed at $d_x = d_y = 1.7$ μm. The lengths of the nanoslits are slightly varied, in order to guarantee a good match between the plasmonic resonance frequency and the vibrational modes of ODT. The corresponding spectra are shown in Figure 5a together with the baseline-corrected vibrational signals in Figure 5b. The spectra reveal that the width has indeed a high impact on the vibrational signal size. For the slit array with the highest value of w, the ODT vibrational bands nearly vanish. With decreasing width the vibrational signal starts to grow and reaches values of more than 14% for a width of approximately w = 50 nm. The extinction of the plasmonic resonance and the vibrational signal size decrease for widths smaller than 50 nm. It is important to mention that the amount of molecules is nearly identical for all measurements. By changing the width, only the surface of the tip ends gets smaller. However, this surface does not contribute to the enhanced signal, because the electric field intensity is negligible at these sites, as shown in Figure 3a. In contrast, the area of the elongated side wall is given by $L \times h$ and therefore is independent of w. The peak-to-peak value of the strongest vibrational band (asymmetric stretching vibration of the methylene group) has been evaluated and is shown in Figure 5c. The double logarithmic plot shows a straight increase of the vibrational signal with decreasing width down to 50 nm. Similar to refs 12 and 20, the general power-law relationship EF $\propto |E|^2 = A \times w^{-m}$ was fitted to the vibrational signal size that is proportional to the EF. The fit gives a result of $m = 1.32 \pm 0.03$, which leads to a relationship of $|E|^2 \propto w^{-1.32}$. Additional to the vibrational signal enhancement, the shift of the resonance frequency due to the ODT layer has been investigated (Figure 5d). A similar behavior is observed; however, the increase of the resonance frequency shift holds also for very small values of w. The same power-law relationship has been used to describe the data, leading to a slightly higher slope, $m = 1.60 \pm 0.07$.

DOI: 10.1021/acsphotonics.5b00390
ACS Photonics 2015, 2, 1489−1497

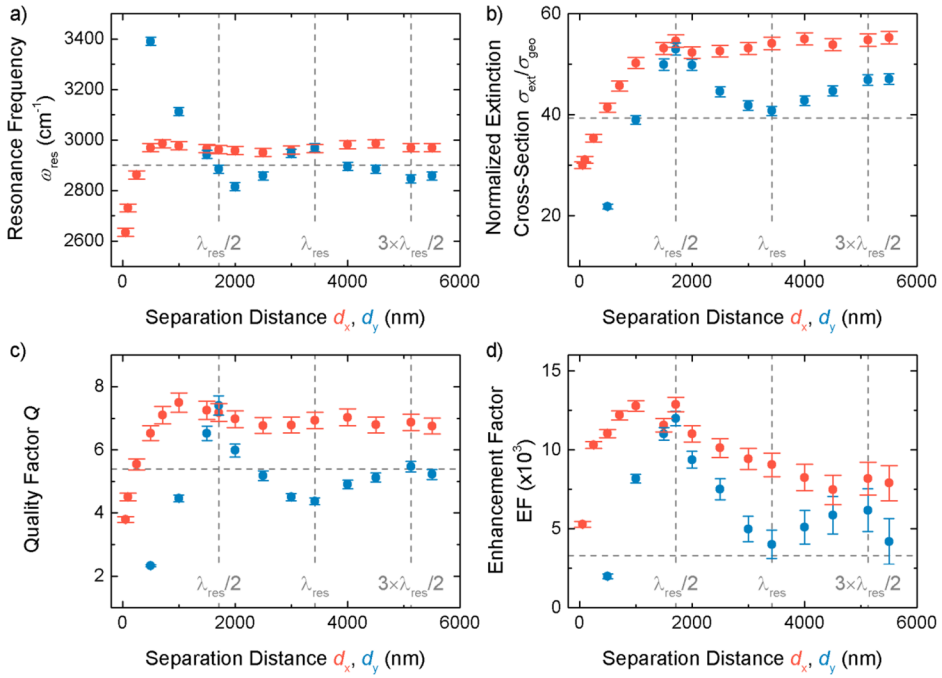

Figure 6. Coupling effects in nanoslit arrays with length L = 1000 nm and width w = 50 nm: Resonance frequency (a), extinction cross section σ_{ext} normalized to geometric cross section σ_{geo} (b), quality factor Q (c), and enhancement of the vibrational signal of the ODT monolayer according to eq 1 (d) of nanoslit arrays with varying separation distances d_x and d_y. A separation distance of $d = \lambda_{res}/2$ (dashed gray line) leads to an increased extinction cross section, quality factor, and vibrational signal, whereas these quantities show a minimum for a separation distance of $d = \lambda_{res}$. The values of a single nanoslit are indicated by the horizontal dashed lines.

The charge distribution of a nanoslit with a nanometer-sized width w is similar to the charge distribution of a nanoantenna dimer: In both cases, opposite charges are separated by a nanometer-sized gap. Therefore, also the consequences of diminishing the gap size g or the width w, respectively, are similar: Both lead to a red shift of the far-field resonance frequency, because the strong attraction across the gap competes against the restoring forces, and also to a decreased far-field intensity, due to a lowered dipole moment. Also the near-field shows similarities: In both cases an increase in near-field intensities is observed by decreasing g or w, respectively. It is also known that the near-field amplitude across a gap of a nanoantenna dimer becomes constant for small gaps,[5] as is also the case for the nanoslit (see also Figure 3a). Therefore, the quantitative influence of the width can be compared to the influence of the gap size of a nanoantenna dimer, where a dependency of the electrical field of the gap size led to similar values of $|E|^2 \propto g^{-0.97}$ for gold nanoantenna dimers[12] or $|E|^2 \propto g^{-1.12}$ for gold bowtie nanoantennas.[20] The value found here is bigger, which clearly indicates the importance of the geometry parameter w. To compare this result with FDTD simulations, the near-field distributions of nanoslit arrays with geometries according to the experiment were calculated and the near-field intensity was integrated over the area inside the slit, where ODT is adsorbed. The result is shown in Figure 5e. The fit of the simulated power-law relationship gives a slope of m = 1.27 ± 0.02, which is in good agreement with the value found for the vibrational signal but, in contrast to the experiment, holds down to very thin slits. It is important to note that quantum effects should come into play for slit widths much smaller than those studied here. The deviation between the measured vibrational signal size and the FDTD simulations for w < 50 nm has another cause. It is explained by imperfect nanoslit arrays: Small amounts of gold inside the nanoslits, either remaining due to a too short etching time or redeposited during the etching process, lead to short-circuited nanoslits (see Figure S2 in the Supporting Information), which then do not contribute to the slit resonance anymore and therefore lower the average extinction as well as the average vibrational signal of the array. This effect only marginally influences the plasmon shift $\Delta\omega_{res}$, which therefore increases even for w < 50 nm. It should be noticed that such observations may be used for the control of a slit array.

So far, the geometry of the nanoslit itself was optimized. In the next step, the response of nanoslit arrays with different x- and y-periodicities is investigated. It is well known that for solid nanoantennas an additional SEIRA enhancement can be achieved if the periodicity $\Delta_{x,y}$ in the x- or y-direction of the array fulfills the condition

$$\Delta_{x,y} = \frac{\lambda_{res}}{n_S} \tag{2}$$

where λ_{res} denotes the resonance wavelength of the individual nanorods and n_S is the refractive index of the substrate.[38−40] Equation 2 considers the interaction with the nearest neighbor in the array in the x- or y-direction.

To investigate this condition also for inverse nanostructures, Figure 6 compares the influence of the separation distance of the nanoslits on the resonance frequency, the normalized extinction cross section, the quality factor, and the EF of the asymmetric stretching vibration of the methylene group of the ODT monolayer. The enhancement factor for the nanoslits is estimated according to eq 1.

Nanoslit arrays with different separation distances in the range 0 < $d_{x,y}$ < 6 μm have been fabricated. The separation distance of one direction was varied, whereas the value for the other direction was fixed to d = 1.7 μm. For separation

DOI: 10.1021/acsphotonics.5b00390
ACS Photonics 2015, 2, 1489−1497

distances in the x-direction smaller than a quarter of the resonant wavelength λ_{res} of an individual nanoslit ($d_x < \lambda_{res}/4$) the resonance frequency shifts toward lower frequencies, whereas it shifts toward higher frequencies if the separation distance in the y-direction decreases below half of the resonant wavelength ($d_y < \lambda_{res}/2$). At a value of $d_y = \lambda_{res}/2$ the slit array shows the lowest resonance frequency. It slightly increases again until the separation distance reaches a value of $d_y = \lambda_{res}$. Whereas this behavior is very pronounced in the y-direction, it is very weak in the x-direction. More interestingly than the resonance frequency is the behavior of the maximum extinction cross section $\sigma_{ext} = (1 - T_{max}) \times (n_s + 1)/2 \times \Delta_x \times \Delta_y$ normalized to the geometric cross section $\sigma_{geo} = L \times w$ and that of the quality factor Q: For a separation of $d = (\lambda_{res}/2) \times i$ with i equal to an odd number, the slit arrays show a high quality factor and a high extinction cross section. For i equal to an even number, the results show a lowered extinction cross section and a smaller quality factor. This effect is much more pronounced in the y-direction than in the x-direction, where the quality factor is nearly doubled. This can be explained by the directional characteristic of a nanoslit, which is dominant in the y-direction. The fact that the coupling for a nanoslit and a nanoantenna array is dominant in the same direction, namely, perpendicular to the long axis of the nanostructure, is a direct consequence of Babinet's principle, which states that the directional characteristic is identical. For small separation distances ($d < \lambda_{res}/2$), both the extinction cross section and the quality factor decrease very fast. The same behavior is observed for the enhanced vibrational signal, where the effect is even stronger. The nanoslit array with an optimum separation distance shows a more than 3 times higher EF compared to the case of the worst coupling. For the investigations of the EF, nanoslit arrays with a good match between the plasmonic resonance frequency and the vibrational frequency have been selected by adjusting the length of the nanoslits. The corresponding spectra are shown in Figure S3 in the Supporting Information. For comparison, the response of an individual nanoslit, with similar geometry, measured using synchrotron radiation, is also indicated in the figure by dashed horizontal lines. The corresponding spectrum is shown in Figure S4 in the Supporting Information. The single nanoslit features a resonance frequency that matches the values for large separation distances, where coupling can be neglected.

The extinction cross section, the quality factor, and the EF show a maximum value close to the value of the resonance frequency minimum at $d_y = \lambda_{res}/2$. This behavior indicates an intense coupling of the nanoslits in the y-direction, stronger than found for nanorods.[38,39] Furthermore, for the nanoantenna array, where the coupling takes places via the substrate, the highest such values are observed for a separation distance of $d_y = \lambda_{res}/n_s$, but for the nanoslits the highest values are found for the separation distances equal to half of the wavelength at resonance, independent of the refractive index of the substrate. The stronger coupling of nanoslits arranged in an array compared to nanoantennas can be explained by different coupling mechanisms. Whereas the nanoantennas couple via photons inside the CaF_2 substrate, the nanoslits certainly couple via a surface plasmon polariton (SPP) at the gold−air interface. For not too small gold thicknesses and frequencies well bellow the plasma frequency, as is the case in the IR, the wavelength of the SPP (λ_{SPP}) at the gold−air interface is similar to the vacuum wavelength indicated in Figure 6, but it is shorter, not matching the observed periodicity, at the interface with the substrate.[41] The coupling via the fields in air is excluded as an important effect because the interferences in nanorod arrays and nanoslit arrays are different.

SUMMARY AND CONCLUSION

In conclusion, we have demonstrated that nanoslit arrays, prepared by EBL with subsequent argon ion etching, feature strong and sharp resonances, tunable over the whole mid-IR spectral range. We showed that these structures represent a beneficial substrate for SEIRA experiments. The comparison to better-known solid nanoantennas proves that the measured average SEIRA signal of the inverse nanostructure is higher compared to a solid nanostructure for the same vibrational layer. We further show that the most important parameter for the near-field enhancement and SEIRA is the width of a nanoslit, having a comparably strong influence on the near-field intensity to the gap size of a nanoantenna dimer. Finally the coupling of slit excitations in the array was optimized for both directions. As a result it turned out that especially the separation distance d_y perpendicular to the slits can lead to an additional SEIRA enhancement if d_y equals half of the resonance wavelength, which reveals a different coupling behavior compared to the solid nanostructures. For SEIRA applications, the optimum geometry parameters of a nanoslit array were determined to be $w \leq 50$ nm and $d_x = d_y = \lambda/2$.

METHODS

Gold Nanoslit Fabrication. Gold nanoslits were fabricated according to the EBL nanopatterning technique: In a first step a 50 nm Au layer was evaporated onto a cleaned $CaF_2(100)$ substrate via thermal evaporation with an evaporation rate of 0.17 Å/s and a background pressure below 2×10^{-7} mbar. Next, 130 nm PMMA (Allresist GmbH, 950 K) was spin-coated at 3000 rpm for 60 s onto the evaporated gold layer. In order to achieve a uniform film thickness, the sample was baked at 150 °C for 3 min. To avoid charging effects during the electron beam patterning, a 10 nm Al layer was thermally evaporated onto the PMMA. Direct writing of the slit structures was carried out using a Zeiss LEO 1530 scanning electron microscope equipped with a Raith EBL system with an acceleration voltage of 15 kV, a beam current of 14 pA, and an exposure dose of 300 $\mu C/cm^2$. Successively, the Al layer was removed in a sodium hydroxide (NaOH) solution and the exposed resist was developed using a conventional methyl isobutyl ketone (MIBK) and isopropyl alcohol (IPA) solution with a mixture ratio of MIBK:IPA = 1:3. The patterned PMMA layer was next used as an etching mask to produce the nanoslit structures in the Au layer: The parts of the Au layer not covered with PMMA were removed employing an argon etching technique with an etching rate of approximately 1.3 nm/s under a pressure of 5×10^{-4} mbar using an ion beam current of 16 mA and an acceleration voltage of 300 V for 90 s. The etching rates of CaF_2 and PMMA are 0.5 and 1.1 nm/s, respectively. Finally, the remaining PMMA was removed using acetone. Subsequent to the nanoslit array fabrication, the samples were characterized by SEM (see Figure 1b) and AFM. The AFM data reveal that the Au layer was completely etched and additionally 25 nm of the underlying CaF_2 substrate was removed (see sketch in Figure 1c).

Binding of Octadecanethiol to Nanoantennas. A self-assembled monolayer of ODT was used to investigate the benefit of nanoslit structures for SEIRA applications. ODT was

DOI: 10.1021/acsphotonics.5b00390
ACS Photonics 2015, 2, 1489−1497

chosen since it forms an almost uniform monolayer of 2.8 nm thickness exclusively on the gold surfaces. In a first step, to remove any organic residues, the sample was cleaned using oxygen plasma for 30 s under a pressure of 0.4 mbar and with a power of 150 W. Next, the sample was exposed to a 1 mM solution of ODT (Sigma-Aldrich, 98%) in ethanol for 24 h. Finally, the sample was rinsed with fresh ethanol to remove unbound ODT molecules and dried with a steady stream of nitrogen. To avoid any degradation of the ODT monolayer, the sample was directly measured after the formation of the ODT layer.

IR Extinction and SEIRA Spectroscopy. IR spectra of nanoslit arrays were recorded utilizing an IR microscope (Bruker Hyperion 1000) coupled to an FTIR spectrometer (Bruker Tensor 27). A polarizer was inserted into the beam path to polarize the light linearly with the electrical field vector along the short axis of the nanoslits. Light was detected using a mercury cadmium telluride (MCT) detector cooled with liquid nitrogen. To avoid any atmospheric influences (water vapor and CO_2 absorption), the whole beam path was purged with dry air. The nanoslit arrays were located by means of white light microscopy, and the arrays were placed in the center of an aperture with a diameter of 70 μm before carrying out the IR measurements. Measurements were carried out in reflectance geometry with a resolution of 2 cm^{-1} and at least 1000 scans. The measurements of the nanoslits were normalized to the reflection of the unstructured gold mirror at a position next to the arrays in order to obtain relative reflectance spectra.

Additional to the measurements of nanoslit arrays, single nanoslits were investigated using IR light from the synchrotron light source ANKA. Measurements were carried out in the same way using an aperture with a diameter of 8.33 μm; however the location of the best measurement position for a single slit is not directly possible by white light microscopy. The localization procedure is explained for example in ref 12.

Numerical Calculations. FDTD simulations (Lumerical FDTD-Solutions v.8.11.337) were carried out in order to study the near-field distributions of nanoslit arrays. To model the array geometry, periodic boundary conditions were chosen in the directions parallel to the substrate surface, whereas perfectly matched layer (PML) boundary conditions were used in the z-direction. The size of the simulation cell in the x- and y-direction is given by the periodicity of the investigated array, whereas the size in the z-direction was chosen in a way that the distance of the nanoslits to the PML is at least one wavelength in both directions. The geometry of the nanoslits was modeled according to Figure 1c. The dielectric function of the gold layer was described by a Drude model with parameters (plasma frequency ω_p = 60 820 cm^{-1}, scattering rate ω_τ = 532 cm^{-1}, and dielectric background ε_∞ = 7.9) derived from our own IR ellipsometric measurements. In a good approximation the CaF_2 substrate was modeled as dispersionless with a refractive index of n = 1.41. The simulation grid was defined by the built-in automesh algorithm with an accuracy level of 4. Additionally a mesh with an accuracy of 1 nm was placed around the nanoslits. The nanoslit arrays were illuminated using a broadband (1900−3900 cm^{-1}) plane wave coming from the air direction with a polarization along the short slit axis. Near-field profiles were recorded using a 3D field profile monitor placed around the nanoslits. In order to reduce the simulation time, all symmetries provided by the system (symmetric boundary conditions in the x-direction and antisymmetric ones in the y-direction) were included in the simulation setup. All simulations were performed taking advantage of the high-performance cluster bwUniCluster.

■ ASSOCIATED CONTENT

Supporting Information

The Supporting Information is available free of charge on the ACS Publications website at DOI: 10.1021/acsphotonics.5b00390.

The IR characterization of a single slit structure measured with synchrotron radiation and IR spectra for several separation distances (PDF)

■ AUTHOR INFORMATION

Corresponding Author

*E-mail: pucci@kip.uni-heidelberg.de.

Notes

The authors declare no competing financial interest.

■ ACKNOWLEDGMENTS

C.H. and D.H. acknowledge financial support by the Helmholtz Graduate School for Hadron and Ion Research. J.V., M.S., and D.H. acknowledge financial support by the Heidelberg Graduate School of Fundamental Physics. F.N. thanks the BW-Stiftung (PROTEINSENS) and the ERC (COMPLEXPLAS) for financial support. We acknowledge SOLEIL for provision of synchrotron radiation facilities, and we would like to thank P. Dumas and F. Jamme for assistance in using beamline SMIS. We acknowledge the Synchrotron Light Source ANKA for provision of synchrotron radiation and instruments at the beamline IR2, and we would like to thank Y. L. Mathis, D. Moss, and M. Süpfle for assistance. We are grateful for computational resources provided by the bwUniCluster of the federal state of Baden-Wuerttemberg, Germany.

■ REFERENCES

(1) Theiss, J.; Pavaskar, P.; Echternach, P. M.; Muller, R. E.; Cronin, S. B. Plasmonic Nanoparticle Arrays with Nanometer Separation for High-Performance SERS Substrates. *Nano Lett.* **2010**, *10*, 2749−2754.

(2) D'Andrea, C.; Bochterle, J.; Toma, A.; Huck, C.; Neubrech, F.; Messina, E.; Fazio, B.; Maragò, O. M.; Di Fabrizio, E.; Lamy de La Chapelle, M.; Gucciardi, P. G.; Pucci, A. Optical Nanoantennas for Multiband Surface-Enhanced Infrared and Raman Spectroscopy. *ACS Nano* **2013**, *7*, 3522−3531.

(3) Kinkhabwala, A.; Yu, Z.; Fan, S.; Avlasevich, Y.; Mullen, K.; Moerner, W. E. Large Single-Molecule Fluorescence Enhancements Produced by a Bowtie Nanoantenna. *Nat. Photonics* **2009**, *3*, 654−657.

(4) Vogt, J.; Huck, C.; Neubrech, F.; Toma, A.; Gerbert, D.; Pucci, A. Impact of the Plasmonic Near- and Far-Field Resonance-Energy Shift on the Enhancement of Infrared Vibrational Signals. *Phys. Chem. Chem. Phys.* **2015**, *17*, 21169−21175.

(5) Aizpurua, J.; Bryant, G. W.; Richter, L. J.; Garcá de Abajo, F. J.; Kelley, B. K.; Mallouk, T. Optical properties of coupled metallic nanorods for field-enhanced spectroscopy. *Phys. Rev. B: Condens. Matter Mater. Phys.* **2005**, *71*, 235420.

(6) Kneipp, K.; Wang, Y.; Kneipp, H.; Perelman, L. T.; Itzkan, I.; Dasari, R. R.; Feld, M. S. Single Molecule Detection Using Surface-Enhanced Raman Scattering (SERS). *Phys. Rev. Lett.* **1997**, *78*, 1667−1670.

(7) Nie, S.; Emory, S. R. Probing Single Molecules and Single Nanoparticles by Surface-Enhanced Raman Scattering. *Science* **1997**, *275*, 1102−1106.

(8) Jiang; Bosnick, K.; Maillard, M.; Brus, L. Single Molecule Raman Spectroscopy at the Junctions of Large Ag Nanocrystals. *J. Phys. Chem. B* **2003**, *107*, 9964−9972.

DOI: 10.1021/acsphotonics.5b00390
ACS Photonics 2015, 2, 1489−1497

(9) Neubrech, F.; Pucci, A.; Cornelius, T. W.; Karim, S.; Garcá-Etxarri, A.; Aizpurua, J. Resonant Plasmonic and Vibrational Coupling in a Tailored Nanoantenna for Infrared Detection. *Phys. Rev. Lett.* **2008**, *101*, 157403.
(10) Brown, L. V.; Zhao, K.; King, N.; Sobhani, H.; Nordlander, P.; Halas, N. J. Surface-Enhanced Infrared Absorption Using Individual Cross Antennas Tailored to Chemical Moieties. *J. Am. Chem. Soc.* **2013**, *135*, 3688−3695.
(11) Hoffmann, J. M.; Janssen, H.; Chigrin, D. N.; Taubner, T. Enhanced Infrared Spectroscopy Using Small-Gap Antennas Prepared with Two-Step Evaporation Nanosphere Lithography. *Opt. Express* **2014**, *22*, 14425−14432.
(12) Huck, C.; Neubrech, F.; Vogt, J.; Toma, A.; Gerbert, D.; Katzmann, J.; Härtling, T.; Pucci, A. Surface-Enhanced Infrared Spectroscopy Using Nanometer-Sized Gaps. *ACS Nano* **2014**, *8*, 4908−4914.
(13) Aouani, H.; Šípová, H.; Rahmani, M.; Navarro-Cia, M.; Hegnerová, K.; Homola, J.; Hong, M.; Maier, S. A. Ultrasensitive Broadband Probing of Molecular Vibrational Modes with Multifrequency Optical Antennas. *ACS Nano* **2013**, *7*, 669−675.
(14) Cubukcu, E.; Zhang, S.; Park, Y.-S.; Bartal, G.; Zhang, X. Split ring resonator sensors for infrared detection of single molecular monolayers. *Appl. Phys. Lett.* **2009**, *95*, 043113.
(15) Chen, K.; Adato, R.; Altug, H. Dual-Band Perfect Absorber for Multispectral Plasmon-Enhanced Infrared Spectroscopy. *ACS Nano* **2012**, *6*, 7998−8006.
(16) Brown, L. V.; Yang, X.; Zhao, K.; Zheng, B. Y.; Nordlander, P.; Halas, N. J. Fan-Shaped Gold Nanoantennas above Reflective Substrates for Surface-Enhanced Infrared Absorption (SEIRA). *Nano Lett.* **2015**, *15*, 1272−1280.
(17) Cetin, A. E.; Etezadi, D.; Altug, H. Accessible Nearfields by Nanoantennas on Nanopedestals for Ultrasensitive Vibrational Spectroscopy. *Adv. Opt. Mater.* **2014**, *2*, 866−872.
(18) Gopalakrishnan, A.; Chirumamilla, M.; De Angelis, F.; Toma, A.; Zaccaria, R. P.; Krahne, R. Bimetallic 3D Nanostar Dimers in Ring Cavities: Recyclable and Robust Surface-Enhanced Raman Scattering Substrates for Signal Detection from Few Molecules. *ACS Nano* **2014**, *8*, 7986−7994.
(19) Chirumamilla, M.; Toma, A.; Gopalakrishnan, A.; Das, G.; Zaccaria, R. P.; Krahne, R.; Rondanina, E.; Leoncini, M.; Liberale, C.; De Angelis, F.; et al. 3D Nanostar Dimers with a Sub-10-nm Gap for Single-/Few-Molecule Surface-Enhanced Raman Scattering. *Adv. Mater.* **2014**, *26*, 2353−2358.
(20) Hatab, N. A.; Hsueh, C.-H.; Gaddis, A. L.; Retterer, S. T.; Li, J.-H.; Eres, G.; Zhang, Z.; Gu, B. Free-Standing Optical Gold Bowtie Nanoantenna with Variable Gap Size for Enhanced Raman Spectroscopy. *Nano Lett.* **2010**, *10*, 4952−4955.
(21) Huck, C.; Toma, A.; Neubrech, F.; Chirumamilla, M.; Vogt, J.; De Angelis, F.; Pucci, A. Gold Nanoantennas on a Pedestal for Plasmonic Enhancement in the Infrared. *ACS Photonics* **2015**, *2*, 497−505.
(22) Liu, N.; Weiss, T.; Mesch, M.; Langguth, L.; Eigenthaler, U.; Hirscher, M.; Sönnichsen, C.; Giessen, H. Planar Metamaterial Analogue of Electromagnetically Induced Transparency for Plasmonic Sensing. *Nano Lett.* **2010**, *10*, 1103−1107.
(23) Hentschel, M.; Weiss, T.; Bagheri, S.; Giessen, H. Babinet to the Half: Coupling of Solid and Inverse Plasmonic Structures. *Nano Lett.* **2013**, *13*, 4428−4433.
(24) Ögüt, B.; Vogelgesang, R.; Sigle, W.; Talebi, N.; Koch, C. T.; van Aken, P. A. Hybridized Metal Slit Eigenmodes as an Illustration of Babinet's Principle. *ACS Nano* **2011**, *5*, 6701−6706.
(25) Zentgraf, T.; Meyrath, T. P.; Seidel, A.; Kaiser, S.; Giessen, H.; Rockstuhl, C.; Lederer, F. Babinet's Principle for Optical Frequency Metamaterials and Nanoantennas. *Phys. Rev. B: Condens. Matter Mater. Phys.* **2007**, *76*, 033407.
(26) Falcone, F.; Lopetegi, T.; Laso, M. A. G.; Baena, J. D.; Bonache, J.; Beruete, M.; Marqués, R.; Mart, F.; Sorolla, M. Babinet Principle Applied to the Design of Metasurfaces and Metamaterials. *Phys. Rev. Lett.* **2004**, *93*, 197401.
(27) Liu, N.; Kaiser, S.; Giessen, H. Magnetoinductive and Electroinductive Coupling in Plasmonic Metamaterial Molecules. *Adv. Mater.* **2008**, *20*, 4521−4525.
(28) Yang, H. U.; Olmon, R. L.; Deryckx, K. S.; Xu, X. G.; Bechtel, H. A.; Xu, Y.; Lail, B. A.; Raschke, M. B. Accessing the Optical Magnetic Near-Field through Babinet's Principle. *ACS Photonics* **2014**, *1*, 894−899.
(29) Cetin, A. E.; Turkmen, M.; Aksu, S.; Etezadi, D.; Altug, H. Multi-Resonant Compact Nanoaperture with Accessible Large Near-fields. *Appl. Phys. B: Lasers Opt.* **2015**, *118*, 29−38.
(30) Rossouw, D.; Botton, G. A. Resonant Optical Excitations in Complementary Plasmonic Nanostructures. *Opt. Express* **2012**, *20*, 6968−6973.
(31) Booker, H. Slot aerials and their relation to complementary wire aerials (Babinet's principle). *Proc. of the IEE, Pt. IIIA* **1946**, *93*, 620−626.
(32) Neubrech, F.; Pucci, A. Plasmonic Enhancement of Vibrational Excitations in the Infrared. *IEEE J. Sel. Top. Quantum Electron.* **2013**, *19*, 4600809.
(33) Neubrech, F.; Kolb, T.; Lovrincic, R.; Fahsold, G.; Pucci, A.; Aizpurua, J.; Cornelius, T. W.; Toimil-Molares, M. E.; Neumann, R.; Karim, S. Resonances of individual metal nanowires in the infrared. *Appl. Phys. Lett.* **2006**, *89*, 253104.
(34) Kats, M. A.; Yu, N.; Genevet, P.; Gaburro, Z.; Capasso, F. Effect of Radiation Damping on the Spectral Response of Plasmonic Components. *Opt. Express* **2011**, *19*, 21748−21753.
(35) Neubrech, F.; Beck, S.; Glaser, T.; Hentschel, M.; Giessen, H.; Pucci, A. Spatial Extent of Plasmonic Enhancement of Vibrational Signals in the Infrared. *ACS Nano* **2014**, *8*, 6250−6258.
(36) Gallinet, B.; Martin, O. J. F. *Ab Initio* Theory of Fano Resonances in Plasmonic Nanostructures and Metamaterials. *Phys. Rev. B: Condens. Matter Mater. Phys.* **2011**, *83*, 235427.
(37) Eilers, P. H. C. A Perfect Smoother. *Anal. Chem.* **2003**, *75*, 3631−3636.
(38) Bagheri, S.; Weber, K.; Gissibl, T.; Weiss, T.; Neubrech, F.; Giessen, H. Fabrication of Square-Centimeter Plasmonic Nanoantenna Arrays by Femtosecond Direct Laser Writing Lithography: Effects of Collective Excitations on SEIRA Enhancement. *ACS Photonics* **2015**, *2*, 779−786.
(39) Weber, D.; Albella, P.; Alonso-González, P.; Neubrech, F.; Gui, H.; Nagao, T.; Hillenbrand, R.; Aizpurua, J.; Pucci, A. Longitudinal and Transverse Coupling in Infrared Gold Nanoantenna Arrays: Long Range Versus Short Range Interaction Regimes. *Opt. Express* **2011**, *19*, 15047−15061.
(40) Adato, R.; Yanik, A. A.; Amsden, J. J.; Kaplan, D. L.; Omenetto, F. G.; Hong, M. K.; Erramilli, S.; Altug, H. Ultra-Sensitive Vibrational Spectroscopy of Protein Monolayers with Plasmonic Nanoantenna Arrays. *Proc. Natl. Acad. Sci. U. S. A.* **2009**, *106*, 19227−19232.
(41) Zayats, A. V.; Smolyaninov, I. I.; Maradudin, A. A. Nano-optics of surface plasmon polaritons. *Phys. Rep.* **2005**, *408*, 131−314.

DOI: 10.1021/acsphotonics.5b00390
ACS Photonics 2015, 2, 1489−1497